Experimental set-up and calibration errors for mapping wave-breaking pressures on marine structures

ANDREA MARZEDDU [(1)], DIMITRIS STAGONAS [(2)], XAVI GIRONELLA [(1)], AGUSTIN SÁNCHEZ-ARCILLA [(1)]

(1) Laboratorio de Ingeniería Marítima (LIM), Universitat Politecnica de Catalunya, Barcelona C/ Jordi Girona 3-1, 08034, Spain, andrea.marzeddu@upc.edu

(2) University College of London, Gower St, London WC1E 6BT, United Kingdom. d.stagonas@ucl.ac.uk

Abstract

Capturing the detailed spatial variation of pressures induced by breaking waves on physical model structures has become possible using a high resolution mapping system. It can provide data with 4 measuring points/cm^2, whereas the denser pressure measurements reported so far, for wave-structure interaction experiments, were limited to 0.4 pressure transducers/cm^2. The paper explores the main parameters affecting the accuracy and errors of pressure data induced by laboratory set-up and system calibration. The quality of pressure maps deteriorates due to cushioning effects associated to air trapped in the sensor during manufacturing. The sensor's response is also shown to depend on the loading conditions. Non-calibrated outputs returned for impact pressures induced by impinging water-jets are more than three times smaller than the outputs recorded for static pressures, and/or for pressures developed when a material less compliant than water comes forcibly in contact with the sensor. Therefore, the calibration settings must be similar to the conditions anticipated in the experiments. To this end, a set-up and calibration methodology, designed specifically for hydraulic model tests with waves breaking on structures, are proposed and discussed in the paper.

Keywords: Pressure mapping system, laboratory set-up, calibration, wave impacts, pressures

1. Introduction

Waves breaking on marine structures induce impulsive pressures (high magnitude and short duration), which have been found to have 5 to 50 times the value of pulsating pressures associated to non-breaking waves, e.g. Allsop et al. (1996). Therefore, significant experimental effort has been devoted to capturing the distribution of pressures stemming from violent wave impacts.

It is generally accepted that the vertical distribution of pressure on a vertical surface varies with breaker type and that peak pressures occur at/near the still water level, Hull and Muller (2002). Nevertheless, experimental evidence suggests a strong horizontal variation in the magnitude of impulsive pressures, the coherence of which remains largely unknown, e.g. Bullock et al., (2007). More recently, Stansberg et al. (2012) used a square matrix of control points, featuring 49 sensors (7 x 7) over an area of 119cm^2 and from here showed the strong, vertical and horizontal, variations in the pressure fields induced by waves breaking on a vertical column. Characteristically, spatially averaged pressures were observed to be significantly reduced compared with local peak values; e.g. a spatially averaged pressure of 74kPa for a test with a maximum pressure peak of 250kPa.

More recently, Stagonas et al. (2016) proposed the use of a Pressure Mapping System (PMS) for detailed recording of wave impact pressure fields. This approach provided pressure measurements with an unprecedented spatial resolution. Compared with Stansberg et al. (2012) the observational mesh increased from 49 measurements over 119cm^2 to 196 measurements over 50.5cm^2. The PMS has been validated against pressure transducers and load cell data and for a range of waves breaking on a vertical seawall, Stagonas et al. (2016). For a large number (120 measurements in each considered case) of breaking and broken waves interacting with a wall, the peak pressure (P_{peak}) profiles and the pressure distribution maps registered by the system agree well with the results acquired using pressure transducers. Although the pressure mapping system tends to underestimate P_{peak}, differences on the mean of the 3rd, 5th and 10th highest P_{peak} fall within ±10% of the average, while for the majority of the measurements the error on the integral of the acting pressures (the acting force compared with the force measured by the load cell) are within ±20%.

The proposed PMS has been recently introduced into hydraulic model tests, but it has been previously employed in a range of geotechnical, biomechanical and sport technology studies, e.g. Palmer et al. (2009), Wilson et al. (2003) and Ouckama and Pearsall (2012). Lu et al. (2013) conducted model scale measurements of ice induced pressures on arctic offshore structures and reported the absence of temperature related effects in their pressure measurements. In contrast, the sudden change in temperature has been shown to introduce errors (thermal peaks) in pressure transducer measurements, e.g. Kim et al. (2015). The majority of experimental results published so far, suggest that the measuring accuracy for contact pressures ranges between 10% and 20% of the applied pressure. However, for the same biomechanical experiment the system's accuracy has been shown to improve by a factor five depending on the selected calibration approach, Brimacombe et al. (2009). The properties of materials in contact with the PMS sensor, the shape of the interface and the loading method also influence the performance of the system. For example, Palmer et al. (2009) described how the generation of shear stresses during geotechnical experiments, which were not accounted for during the calibration, could reduce the measurements' accuracy by up-to 40%. Overall, the PMS response and performance have been shown to depend on the experimental protocol and therefore the system's behaviour should be investigated for each different application.

In this paper the PMS's performance and accuracy are evaluated extensively for hydraulic model tests dealing with wave-structure interactions. Section 2 describes the system and the experimental details regarding equipment and methods are presented in Section 3. Results characterizing different error sources are reported in Section 4 and the work concludes in Section 5, suggesting an optimum approach for the system set-up and applications within hydraulic model tests with breaking waves.

2. The pressure mapping system

The TekScan I-Scan™ pressure mapping system (PMS) used in the present study consists of two main components, the data acquisition hardware and the tactile sensor(s), which are contrasted with the data acquisition board and the pressure transducer, respectively. The primary differences between the PMS data acquisition hardware and other data acquisition boards are related to the fixed 8bit resolution and the capacity to collect data from up-to eight sensors simultaneously.

In addition, the PMS sensors are drastically different from pressure transducers. Each sensor consists of two thin, flexible polymer sheets with electrical strip patterns (conductors) deposited on them. The opposing interior faces contain rows and columns of resistive ink, which covers the conductors. Rows and columns intersect at grid points forming sensing cells, which are referred to as sensels, Figure 1 (a) and (b). The resistance of every sensel is an inverse function of the applied pressure and pressure-free sensels return the maximum resistance. When a pressure is applied on the sensor, the resistance of loaded sensels reduces, while the signals returned by each sensel are read sequentially. As shown in Figure 1 (b), the overlap of rows with columns results in 'live' and 'dead' areas in every sensor, where the applied pressure is (respectively) measured or not. The presence of active and inactive areas influences how sensors respond when a load is exerted, using materials with different degrees of compliance, such as rubber or water. For the same load, the relation between the deformation (compliance) of the material interacting with the sensor and the distribution of pressures registered by this sensor is illustrated in Figure 2.

All sensors have a thickness smaller than 0.1mm but the spacing between rows and columns can be as small as ~0.5mm, with sensors of different dimensions available. To give an example, the sensor used in the present study has 7.11 × 7.11cmxcm dimensions, with a resolution of 3.9 sensels per cm^2 (196 sensels over $50.5cm^2$). The sensor employed in large scale wave-structure interaction experiments is 58.97 × 48.81cmxcm, with 1 sensel per cm^2 (2080 sensels over

2081cm^2), see Figure 3 (c) and Stagonas et al. (2014). The key differences stemming from dimension and resolution are the maximum possible sampling frequency and the presence/absence of ‘ventilation’ channels. The sampling frequency depends on the number of sensels sampled. Therefore the sensor with 196 sensels can be sampled at a maximum frequency of 4kHz per sensel, whilst for the larger sensor (2016 sensels) the highest sampling frequency possible is 680Hz per sensel. Sampling rates of up-to 20kHz per sensel is also possible for sensors with 44 sensels. During manufacturing air is trapped between the two substrates of every sensor so that for sensors with larger dimensions the amount of entrapped air is high enough to endanger the sensor’s integrity, especially when high magnitude loads are applied. ‘Ventilation’ channels act as outlets for the trapped air preventing permanent damage to the sensor.

Before using any of the tactile pressure sensors, the manufacturer recommends a procedure which includes conditioning, equilibration and calibration of the sensor, Tekscan (2008). Conditioning supposes loading the sensor to various levels prior to the experiments, and it has been reported to improve the overall performance and repeatability. In particular, conditioning has been shown to minimize the drift and hysteresis observed otherwise in pressure records, e.g. Palmer et al. (2009). Both drift and hysteresis are time dependent effects, which have not been observed to occur for pressure application times smaller than 2sec, Stagonas et al. (2016). In the present study, sensor conditioning was performed using a vacuum pump to apply different levels of uniform pressure, with the aim of spanning the pressure range of the sensor.

The same approach has been employed to equilibrate the sensor. Equilibration constitutes a normalisation procedure aiming to compensate for differences in sensitivity between sensels, due to manufacturing or weathering. For each sensel a scale factor is determined so that its digital output equals the average digital output of all loaded sensels. Considering a uniform pressure, sensels with a higher / lower original output are assigned a correction factor decreasing / increasing their output. For multiple pressure levels, spanning the pressure range of the sensor equilibration matrices produces a set of correction factors, which can be used before, during or after the experiment.

Following equilibration, the PMS pressure sensors can be calibrated using one or two different uniform pressure (load) levels, Tekscan (2008). The pressure-free (unloaded) sensor is assumed to have zero output and the line connecting the zero point to the calibration point is used for reference (one level). For the two-level calibration the power law equation connecting the calibration points is computed and applied. Nevertheless, calibration approaches employing more than two points have been reported to result in up-to five times more precise pressure measurements, with variations between different applications, Wilson et al. (2006), Brimacombe et al. (2009), Ouckama and Pearsall (2011) and Ouckama and Pearsall (2012).

It is, however, noted that set-up and calibration approaches differ drastically between studies. More importantly, significant alterations in the system's performance and accuracy have been reported when the measuring conditions were different from the calibration conditions, Ferguson et al. (1993).

In the present paper, an experimental rig has been specifically developed to explore the limitations related to the manufacturing and material properties of the PMS sensor. Different set-up and calibration approaches, together with a range of loading methods have been considered to facilitate a direct application to wave-structure interaction experiments. In particular, the effects of entrapped air and the system's response have been studied for static and dynamic pressures, corresponding to still water column and impinging water-jet experiments with water and a less compliant material. From here the implications of calibration for assessing errors and data reliability have been derived.

3. Methodology

3.1. The experimental apparatus

The experimental rig is presented in Figure 4 (a). The sensor is fixed on an aluminium plate supported by a pair of HBM Z6FC3 bending beam load cells, arranged in a series. The rig was specifically designed to allow simultaneous measurements of loads (with the load cells) and pressures (with the PMS). The information on the size of the loaded area available in the PMS records is then used to compute the total load acting on the sensor and to contrast it with load cell measurements. A series of ad-hoc tests with a mallet (nylon hammer) showed that the natural frequency of the plate load cell was around 50 Hz, significantly lower than the frequencies of the water-jet induced pressure pulses (ranging approximately from 500 to 2000 Hz). This has confirmed the load cell-aluminium plate arrangement is stiff enough to prevent undesired dynamic excitation.

The 9500 pressure mapping sensor has been used in the current work. This sensor has 196 sensels arranged in 14 rows and 14 columns, covering an area of 50.5cm^2 without ‘ventilation’ channels. For all experiments each sensel was sampled with the maximum possible rate of 4kHz. According to the manufacturer, uniform static loads acting on parts of the sensor are used to define the pressure range, which for the sensor of Figure 3 ranged from 0 to 35kPa. Overloading without damaging the sensor is possible but once the pressure acting on a sensel exceeds the upper pressure limit (e.g. 35kPa), this sensel record is capped and it is considered saturated. Further increases in the pressure will not be registered and the maximum digital output (255) will be returned as long as the sensel is overloaded. However, the experimental results presented in Ramachandran et al. (2013) illustrate that when non-uniform and non-static (dynamic) pressures are acting on a PMS sensor, then sensel can be loaded past the upper limit without reaching saturation. Therefore, for the rest of this paper the pressure range assigned to the sensor by the manufacturer will be referred to as the nominal pressure range.

Since the PMS sensors are not water-proof, some water proofing is required. To this end, the sensor was placed in a 0.05mm thick vacuum bag (Minimatic bag). Creating an additional protective layer with a 0.05mm thick nylon film (NBF-740-LFT 0.05 mm) was found to prevent water from leaking into the vacuum bag during long duration experiments, Figure 5. Air trapped between the sensor bag and the foil may yield unwanted cushioning effects and thus a vacuum pump was used to extract it. The pump was connected to the rig through a tapped hole located in the side of the sensor and under the film, Figure 5. The vacuum pump was also used to apply different levels of pressure for conditioning and equilibrating the sensor. A 30th order finite impulse response filter (designed in Matlab) was used to remove the noise induced in the measurements by the operation of the pump. This was deemed necessary as the physical isolation of the pump from the system, e.g. by using different a power source with an incorporate hardware filter, did not result in significant improvements. The pump noise polluted frequencies of about 25Hz, thus the filter used for post-processing the data had stopband attenuation limits at 18Hz and 30Hz.

Three different versions of the experimental apparatus presented in Figure 4 have been employed to explore the sensor response to dynamic loads (using water and a less compliant medium) and to static loads. For the generation of impinging water jets, two 0.25m long PVC tubes with diameters Ø = 0.019m and Ø = 0.032m, were placed at a distance of d = 0.8m above the sensor, Figure 4 (a). The tubes were filled with water to a depth of h = 0.07m and the sensor facing the tube end was shielded with a manually controlled gate. Releasing the gate resulted in water jets impacting on the sensor. The shape and magnitude of impact pulses and the dimension of the impact area were found to be a function of d, h and Ø (Figure 4 (a)). In particular, the size of the impact area increased with Ø, while increasing d and h increased the pressure magnitude and decreased its rise time (defined as the time required for the pressure to reach its peak from zero). These findings are consistent with previously published works, e.g. Tu and Woo (1996). In large scale experiments with waves breaking on a seawall, pressure pulses have an idealised triangular shape, Cuomo et al. (2010). The values of d, h and Ø used in the current study yielded impact pressure pulses with triangular shapes and characteristics (namely, rise times and peak magnitudes) similar to those acquired in experiments reproducing Cuomo et al. (2010)‘s arrangement in small scale, Stagonas et al. (2016).

Figure 4 (b) presents the pendulum-like arrangement designed to generate impact pressures using a material less compliant than water, see also Ramachandran et al. (2013). The structure consisted of an articulated arm, a 47x47 mm steel plate fixed on a HBM Z6FC3 load cell, and a

3cm thick (300pores per inch) porous sponge layer attached on the side of the plate in contact with the sensor. The sponge layer protected the sensor from direct contact with the steel plate and, more importantly, it provided an interface which during impact was less adaptable than water. In contrast to dynamic pressures, water was the only medium used to examine the sensor's response to static pressures. For this purpose, a 3m high column with 0.15m diameter, was fixed on the sensor and measurements were conducted with 13 water depths ranging from 0.2 to 2.6m with intervals of 0.2 m, Figure 4 (c). Examples of the static and impact pressure pulses are presented in Figure 6 (a) and (b) respectively.

3.2. The calibration methodology

In the majority of previous studies calibration followed conditioning and equilibration, with emphasis on the resultant load rather than the load / pressure distribution. As such, the calibration procedure considered the total response of the tactile pressure sensor and not the response of each individual sensel, e.g. Brimacombe et al. (2009). Nonetheless, this approach is of little value for wave-structure interaction experiments, where the focus tends to be on capturing the impact pressure distribution. Therefore, the arrangement above described has been specifically designed for the calibration of individual sensels, based on the following (new) calibration methodology:

- The sensor is subject to impinging water-jets and the resulting loads are simultaneously measured by the sensor and the load cells.
- For each impact, the peak of the mean pressure acting on the sensor is obtained. The time history of the mean pressure is calculated from the fraction of load cells data corresponding to the loaded area, estimated from the pressure mapping system, Eqs. 1 and 2.
- A weighting factor is computed for each sensel by considering its digital output and the mean digital output of all sensels, Eq. 3.

- The pressure acting on each sensel is then estimated using the weighting factor calculated in the previous step, Eq. 4. Any sensel can now be calibrated using its own digital output and the calculated acting pressure.

For the present study 300 water-jet impacts were considered, enabling a multi-level calibration for any of the 196 sensels of the sensor. In the remainder, the individual sensel calibration is denoted as sensel-by-sensel calibration. Nevertheless, it is also possible to use all the data collected and compute a single calibration function for the whole sensor; this procedure is similar to other proposals in the existing literature and for the rest of the current work it will be referred to as global calibration. However, it should be noted that for global calibration it is necessary to have an equilibrated sensor.

The size of area A highlighted in Figure 7 (c) and (d) is calculated as**:**

$$A = N * A_{sensel} \qquad \text{Eq. 1}$$

where

- N: is the number of active sensels at the time of the force peak in the time history recorded from the load cells
- A_{sensel}: is the sensel area, equal to 26 mm^2

From here

$$P_{LC} = \frac{F_{PLC}}{A} \qquad \text{Eq. 2}$$

where

- F_{PLC}: is the peak force measured by the load cell
- P_{LC}: is the mean pressure acting on the tactile sensor at the time F_{PLC} occurs

The contribution of each sensel is then computed as:

$$C_{i,j} = \frac{DO_{i,j}}{\overline{DO}} \qquad \text{Eq. 3}$$

where

- $C_{i,j}$: is the weighting factor of (i,j) sensel, with i = 1…14 and j = 1…14.
- $DO_{i,j}$: is the digital output of the sensel
- $\overline{DO}$: is the mean of the digital output of all sensels active at the time instant the peak force is recorded by the load cells.

The combination of Eqs. 1 to 3 gives the weighted pressure, $P_{i,j}$, acting on the (i,j) sensel:

$$P_{i,j} = C_{i,j} * P_{LC} \qquad \text{Eq. 4}$$

Figures 7 (a) and (b) present examples of the weighted pressure ($P_{i,j}$) plotted over the digital output for all and each individual sensels, respectively. The non-calibrated map reported by the system at the time of the impact force peak is also shown in Figure 7 (c), while in Figure 7 (d) the map of the weighted factors for the same impact and time instant is shown.

4. Experimental results

In order to test the response of the PMS and propose a functional calibration methodology, a series of tests are performed. Specifically:

- response of the PMS for sensors with and without ventilation channels
- response of the PMS to mediums with different compliance levels
- response of the PMS to static and dynamic loads

Following the identification of the optimum calibration conditions, the option to individually calibrate each and every sensel is compared with a global calibration for which a calibration function is defined and used for all sensels. To this end, the performance of linear and higher order calibration function is also evaluated.

4.1. Entrapped air effects

To explore the effects of entrapped air a series of tests have been conducted, using the sensor as provided by the manufacturer and then with 'ventilation' channels (Figure 1a) cut on its sides, where the entrapped air was evacuated using the vacuum pump. This modified sensor will be referred to as perforated and the original sensor as non-perforated. The use of the pump induces a constant uniform pressure which can be removed from the measurements either during the experiment or during the data post-processing. For all tests here reported a vacuum level of 40 kPa was found to be the minimum required to remove most of the air trapped in the sensor and water-proofing arrangement (Figure 5) and was thus selected. Previously, Ramachandran et al. (2013) reported negligible differences in the response of a pressure sensor loaded with the same uniform pressures but for different initial vacuum levels.

Results collected from 300 impacts on the non-perforated and perforated sensors, using the pendulum-like arrangement of Figure 4 (b), have been compared, with emphasis on the distribution of impact pressures, the loaded area characteristics and the sensels response. For these tests pendulum induced impacts were preferred to water-jet impacts, because for the former the size of the impact area is known a-priori and thus a comparison with the area reported by the PMS becomes easier and more direct.

Figure 8, presents some representative examples of PMS maps, recorded for similar loading conditions by the non-perforated (Figure 8 (a)) and perforated sensors (Figure 8 (b)). Cushioning effects due to the entrapped air can be observed in Figure 8 (a), where no-pressure zones are reported within the loaded area. In the absence of ventilation channels, the air contained in the sensor is trapped between the substrates and limits (or fully prevents) the contact of some rows with the sensitive columns (for some parts of the sensor). This leads to zones within the loaded area with erroneously small or even nullified pressure records. In contrast, when the air is removed the pressure distribution is reported in detail and the no-pressure zones disappear, Figure 8 (b).

The size of the area calculated using measurements acquired before (crosses) and after (circles) perforating the sensor is compared for different acting pressures in Figure 9 (a). Although a similar trend – area increases with pressure– can be observed, the surface measured using the non-perforated sensor is consistently lower than the pendulum's steel plate area, which is approx. 2200mm^2. In contrast, the impact area for the perforated sensor is seen to compare well with the pendulum's area, albeit with some differences for lower P_{LC}, attributed to the deformation of the sponge layer covering the pendulum's plate. As the magnitude of the applied pressure increases so does the deformation of the sponge layer and thus the size of the loaded area reported by the PMS converges to that of the steel plate.

The digital outputs of all sensels are plotted against the weighted pressure (Eq. 4) for tests with the non-perforated (grey crosses) and perforated (black circles) sensors, Figure 9 (b). For the same $P_{i,j}$ the sensels of the perforated sensor are seen to report significantly higher digital outputs and the scatter of the data reduces drastically. Characteristically, the steepness of the linear fit line (grey and black lines in Figure 9 (b)) reduces by 75% for the tests with the perforated sensor.

4.2. Material characteristics effects

The performance of the PMS for two different nonlinear materials has been also explored. As described above, nonlinear materials result, for the same loading conditions, in less uniform distribution of pressures on the sensor. Materials with different properties (e.g. compliance) yield drastically different responses for the sensor, which requires that experimental conditions should be reproduced as precisely as possible during the calibration. Therefore, in this section pendulum impacts (sponge layer interface) are compared with water-jet impacts. For the former a sponge layer interface is formed between the sensor and the pendulum, while the latter corresponds to the conditions in hydraulic model tests.

The digital outputs of all sensels are plotted against the weighted pressures in Figure 10 (a); results for water-jet impacts are presented with black circles and with grey crosses for the pendulum. The sensel responses are significantly steeper for the former and, for example, an acting pressure of 10kPa yields digital outputs between 5 and 15 instead of 75 to 85 for the pendulum impact. This trend was consistent for the considered range of impacts and thus for hydraulic model tests a water based calibration should be preferred over other approaches involving less compliant materials.

Interestingly enough, even when water-jet induced pressures exceed the nominal range of the sensor (35kPa) overload (saturated) sensels are not reported. In contrast, using the linear fit function for the pendulum impacts (grey line in Figure 10 (a)) the sensor reaches saturation for a pressure around 30kPa, which is close to the sensor's nominal upper limit of 35kPa. This behaviour for the pendulum impacts corroborate former results reported in Ramahandran et al. (2013). A more comprehensive assessment of the exact pressure range for the perforated sensor falls outside the scope of the present work.

4.3. Dynamic and static loads

Using static loads to calibrate pressure transducers for hydraulic model tests with breaking waves is not an unusual practice. This section explores the suitability of this approach for the pressure mapping system, looking at its response as a function of the applied (static and dynamic) loads.

The modified experimental arrangement of Figure 4 (c) was used to record the sensor's response to static loads. The digital output of all sensels (grey crosses) is plotted against the static pressures ($P_{i,j}$) corresponding to the 13 water depths tested, and it is compared with water-jet impact results in Figure 10 (b). For the water-jet tests the sensor was not equilibrated, and non-equilibrated data have been also used for static pressures. Drastic differences can be observed between the two loading conditions. For example, considering weighted pressures ranging from 10kPa to 20kPa, the digital output for all sensels is seen to be between 15 and 30. In contrast, when similar (magnitude) static pressures act on the sensor, the recorded digital outputs are from 60 to 120. Once again, significant differences can be appreciated for the two loading cases and clearly a static load based calibration is not suitable for experiments considering wave impacts.

4.4. Calibration approach effects

For most previous work, sensor calibration follows conditioning and equilibration and then a unique function is defined to convert the digital output of all sensels to load / pressure units.

In this approach equilibration is used to reduce the scatter in the responses of different sensels subjected to the same pressure and serves to assess calibration induced errors. However, and to the best of the authors knowledge, it remains largely unknown if normalizing (equilibrating) the sensels will induce further errors in the pressure distribution map.

The sensel-by-sensel calibration approach here described does not require equilibrating the sensor and can be compared with the global calibration approach. To this end, only water-jet impacts are considered and suitable calibration functions are computed for each of the 196 sensels. The sensor is then equilibrated and a single (global) function is defined, which is used to calibrate the output of all sensels. For each sensel the linear function with the best fit to the registered data is selected and the slope and R^2 values of all functions are compared with the slope and R^2 values for the global linear function, Table 1. Although relatively satisfactory R^2 values are reported for all cases, the slope for the global function is 0.97, which differs from the minimum, mean and maximum slope calculated for the linear functions of the sensel-by-sensel calibration. This means that such calibration errors will be inevitably introduced whenever a global function is selected to calibrate all sensels.

The resulting calibration-based errors are explored in Figure 11, where the plotted loads have been computed by integrating the pressures recorded by each sensel. In particular, the load peaks calculated using the global function ($F_{p\text{-Global Calib}}$) are plotted over the peaks of the load calculated using the sensel-by-sensel approach ($F_{p\text{-SbS Calib}}$). For the majority of tests, the global calibration is seen to result in underestimation of the force peaks by about 10%, while for a limited number of cases force peaks are overestimated by about 5%. From these results, a global calibration approach should not be completely disregarded as it offers a less laborious albeit less accurate option.

Having determined that the sensel-by-sensel calibration is more accurate, it is convenient to examine the calibration induced errors associated with the characteristics (e.g. linear and nonlinear) of the selected calibration function. A consensus has been reached in the literature that user defined functions yield more accurate results than many calibration functions recommended by manufacturers, e.g. Brimacombe et al. (2009). Hence three, user defined, calibration functions are now considered. They comprise linear, power-law, and 2nd order polynomial functions with the best fit to the collected data for every sensel. The number of calibration points and R^2 values are presented in Figures 12 (a) to (d). In addition, the R^2 minimum, mean and maximum and the Root Mean Square Error (RMSE) are summarized in Table 2.

None of the three functions is seen to provide a clearly better fit and practically identical RMS errors are reported, Table 2. The integral of the pressures acting on each sensel has been then calculated for every function and the results are compared with the load cell measurements. For forces ranging from 5N to 50N the minimum, mean±std and maximum, and the RMS errors are shown in Table 3. Once again, the performances of the three functions are observed to be statistically indistinguishable.

Nevertheless, the use of nonlinear functions for sensor calibration is recommended if pressures spanning the sensor's nominal range are anticipated in the experiments, Tekscan (2008). Recently, Stagonas et al. (2016) employed a sensel-by-sensel approach to calibrate the sensor for experiments with waves breaking on a vertical wall and reported nonlinear functions to result in more accurate data. In particular, pressure and load (the integral of pressures) measurements conducted with the PMS were compared with measurements conducted with pressure transducers and load cells. Compared with a 2nd order polynomial, a power law function yielded the most satisfactory results. Considering the mean of the pressure peaks, differences between the PMS and pressure transducers ranged between ±15%, while the average values of the 3, 5 and 10 highest pressure peaks differed by up to ±10%. Furthermore, the discrepancy between the integral of the pressures acting on the sensor and simultaneous load cell measurements was less than ±20%.

From here it can be argued that nonlinear functions describe better the response of the sensels, especially when acting pressures are smaller than about 15% and higher than about 85% of the sensor's nominal limits (for this study upper value of 35kPa), Figure 13; the power law and the 2nd order polynomial functions are also plotted over the data of Figure 7 (b). However, a limitation of the present work refers to the small number of calibration data available for pressures smaller than approximately 5kPa and higher than about 40kPa. For this purpose an alternative approach was devised to examine the errors induced from an insufficient description of sensel responses at both ends of the calibration range. For every impact, the integral of pressures acting on the senor is calculated and the peak of the computed force is compared with the peak of the force measured from load cells. The error is then calculated as:

$$E_{\%} = \frac{F_{LC} - F_{TEK}}{F_{LC}} \cdot 100 \qquad \text{Eq. 5}$$

where:

- F_{LC} : is the peak of the force measured by the load cells
- F_{TEK} : is the peak of the force calculated using the pressure sensor measurements
- $E_{\%}$: is the percentage of the error

The integral of pressures includes measurements spanning the full calibration range but previous work suggests the PMS should yield more accurate results when the applied pressures exceeded 10% of the upper-bound sensor pressure, e.g. Palmer el al. (2009) and Ouckama and Pearsall (2012). Therefore remains the question of how the error reported by Eq. 5 is affected by the number of sensels subject to pressures smaller than 10% of the upper-bound sensor pressure.

To answer this question, the error of Eq. 5 was multiplied by the fraction of sensels reporting pressures lower than 10% of the highest pressure recorded in all tests (60 kPa) over the number of sensels reporting pressures higher than 10% of the highest pressure, Eq. 6. Since the nominal upper-bound of the sensor was clearly exceeded in all our tests, the highest pressure reported was considered a more suitable option.

$$\frac{N_{10\%}}{N_{90\%}} * E_{\%} \qquad \text{Eq. 6}$$

where,

- $N_{10\%}$: is the number of sensels reporting pressures smaller than 10% of the highest pressures recorded in all tests.
- $N_{90\%}$: is the number of sensels reporting pressures higher than 10% of the highest pressures recorded in all tests
- $E_{\%}$: is the error calculated with Eq. 5

In Figure 14, the largest error (>20% and <-20%) between the calculated (PMS) and the measured (load cells) forces is reported for the largest $N_{10\%}$. In other words, when the number of pressures with peaks lower than 10% of the highest peak pressure increases, the error in the integral of pressures also increases. On the other hand, as $N_{90\%}$ increases the error reduces and gradually becomes less than 10%. In accordance with previous work, e.g. Palmer el al. (2009), a tendency is also observed for the calibration error to reduce as the peak of the applied pressure increases.

5. Conclusions

The present study has explored the main parameters affecting the performance and accuracy of a pressure mapping system intended for applications in hydraulic model tests with waves breaking on structures. The experimental arrangement used was specifically designed to test the sensor's response to different loading conditions and calibration approaches. The air trapped in the sensor, the properties of the medium in contact with the sensor, and the type (static or dynamic) of applied pressures have been identified as the most influential parameters.

In particular, cushioning effects due to the entrapped air resulted in a significant deterioration in the quality of the impact pressure maps recorded by the system. Compared with the impact area of the pendulum-like arrangement, the size of the contact area reported by the PMS was in average 60% smaller. When the air was removed the agreement between impact and contact area improved in average up to 95%.

The response of the air-free sensor was then investigated for impacts induced using the sponge layer and water-jets. The digital output of all sensels is drastically different when a more compliant material is in contact with the sensor. Compared with the sponge layer tests, water-jet impacts resulted in more than four times smaller outputs for sensels subject to similar pressure levels. Considering the water-jet impacts, the loading range of the modified (air-free) sensor was also found to exceed the nominal upper bound (suggested by the manufacturer) by more than 3 times, corroborating previous results in Ramahandran et al. (2013). Drastic differences in the sensor's response are also reported between static and dynamic loading conditions. Sensels subject to pressures induced by a static water column return digital outputs more than four times higher than the outputs from water-jet impact pressures (with the same peak magnitude).

From these analyses a new calibration methodology has been proposed. Compared with any previously recommended approach the calibration of individual sensels becomes possible and the need to equilibrate the sensor can be circumvented. Calibrating each sensel separately is shown to increase the accuracy of the measurements, especially when the focus is on the variations in the impact induced pressure field. A simplified, less cumbersome, global calibration approach is also proposed for tests where the need for accuracy is not so strict.

In agreement with existing literature, user defined calibration functions are reported to reduce the error in most measurements but, in contradiction to previous work, linear and nonlinear fit functions are seen to yield statistically indistinguishable results. Nevertheless, for experiments with waves breaking on a seawall the power law calibration was seen to reduce the calibration error. Specifically, Stagonas et al. (2016) presented tests where pressure and force peaks measured with the PMS sensor ranged between ±15% and ±20% of those measured using pressure transducers and load cells.

In summary, this is the first evaluation of the set-up and calibration induced errors for a pressure mapping system used in hydraulic model tests with waves breaking on structures. Removing the air trapped in the pressure sensor and using water-jet impacts to conduct a sensel-by-sensel calibration is one of the clear recommendations. Employing a nonlinear function (in particular a power law) is also suggested when the range of experimental pressures is expected to span the loading range of the sensor. Finally, the accumulated experience using the PMS indicates that the water-proofing set-up described in the current paper can be successfully employed in small and large scale breaking wave-structure interaction experiments.

Acknowledgments

This study was supported by the EU Programme H2020 project Hydralab+ (contract number GA654110). Partial support was received from the Ministry of Education, Culture, and Sports, Spain (FPU grant AP-2010-4641) and by the *Secretariad'UniversitatsiRecerca del Dpt. d'EconomiaiConeixement de la Generalitat de Catalunya* (Ref 2014SGR1253).

References

Allsop, N. W. H., Vicinanza, D., & McKenna, J. E. (1996). Wave forces on vertical and composite breakwaters (Vol. Strategic).

Brimacombe, J. M., Wilson, D. R., Hodgson, A. J., Ho, K. C., & Anglin, C. (2009). Effect of calibration method on Tekscan sensor accuracy. Journal of Biomechanical Engineering, 131(3), 34503.

Bullock, G. N., Obhrai, C., Peregrine, D. H., & Bredmose, H. (2007). Violent breaking wave impacts. Part 1: Results from large-scale regular wave tests on vertical and sloping walls. Coastal Engineering, 54(8), 602–617. https://doi.org/10.1016/j.coastaleng.2006.12.002

Cuomo, G., Allsop, N. W. H., Bruce, T., & Pearson, J. (2010). Breaking wave loads at vertical seawalls and breakwaters. Coastal Engineering, 57(4), 424–439. https://doi.org/10.1016/j.coastaleng.2009.11.005

Ferguson-Pell, M., & Cardi, M. D. (1993). Prototype development and comparative evaluation of wheelchair pressure mapping system. Assistive Technology, 5(2), 78–91.

Hull, P., & Müller, G. (2002). An investigation of breaker heights, shapes and pressures. Ocean Engineering, 29, 59–79. https://doi.org/10.1016/S0029-8018(00)00075-5

Kim, S.-Y., Kim, K.-H., & Kim, Y. (2015). Comparative study on pressure sensors for sloshing experiment. Ocean Engineering, 94, 199–212. https://doi.org/10.1016/j.oceaneng.2014.11.014

Lu, W., Serré, N., Høyland, K., & Evers, K. (2013). Rubble Ice Transport on Arctic Offshore. In Proceedings of the 22nd international conference on Port and Ocean Engineering under Arctic conditions. Espoo, finland.

Ouckama, R., & Pearsall, D. J. (2011). Evaluation of a flexible force sensor for measurement of helmet foam impact performance. Journal of Biomechanics. Elsevier.

Ouckama, R., & Pearsall, D. J. (2012). Impact performance of ice hockey helmets: head acceleration versus focal force dispersion. Proceedings of the Institution of Mechanical Engineers, Part P: Journal of Sports Engineering and Technology. SAGE Publications.

Palmer, M. C., O'Rourke, T. D., Olson, N. a., Abdoun, T., Ha, D., & O'Rourke, M. J. (2009). Tactile Pressure Sensors for Soil-Structure Interaction Assessment. Journal of Geotechnical and Geoenvironmental Engineering, 135(11), 1638–1645. https://doi.org/10.1061/(ASCE)GT.1943-5606.0000143

Ramachandran, K., Schimmels, S., Stagonas, D., & Müller, G. (2013). Measuring Wave Impact on Coastal Structures with High Spatial and Temporal Resolution--Tactile Pressure Sensors a Novel Approach. In 35th IAHR World Congress, Chengdu, China.

Stagonas, D., Lara, J. L., Losada, I. J., Higuera, P., Jaime, F. F., & Muller, G. (2014). Large scale measurements of wave loads and mapping of impact pressure distribution at the underside of wave recurves.

Stagonas, D., Marzeddu, A., Gironella, X., & Sánchez-Arcilla, A. (2016). Measuring wave impact induced pressures with a pressure mapping system. Coastal Engineering, (112), 44–56.

Stansberg, C., Berget, K., Graczyk, M., Muthanna, C., & Pakozdi, C. (2012). Breaking wave kinematics and resulting slamming pressures on a vertical column. In Proceedings of the ASME 2012 31st International Conference on Ocean, Offshore and Arctic Engineering. Rio de Janeiro, Brazil.

Tekscan, I. (2008). I-Scan and High speed I-Scan User manual, 1–11.

Tu, C. V., & Wood, D. H. (1996). Wall pressure and shear stress measurements beneath an impinging jet. Experimental Thermal and Fluid Science, 13(4), 364–373. https://doi.org/10.1016/S0894-1777(96)00093-3

Wilson, D. C., Niosi, C. A., Zhu, Q. A., Oxland, T. R., & Wilson, D. R. (2006). Accuracy and repeatability of a new method for measuring facet loads in the lumbar spine. Journal of Biomechanics, 39(2), 348–353.

Wilson, D. R., Apreleva, M. V, Eichler, M. J., & Harrold, F. R. (2003). Accuracy and repeatability of a pressure measurement system in the patellofemoral joint. Journal of Biomechanics, 36(12), 1909–1915.

Table 1: Linear calibration coefficient and R2 values for the global and sensel-by-sensel approaches.

Calibration y=ax	**a**				**R2**			
Equilibration and global calib	0.97				0.98			
	min	**max**	**mean**	**std**	**min**	**max**	**mean**	**std**
No equilibration and calib sbs	0.9	1.29	1.03	0.02	0.81	1	0.94	0.01

Table 2:R2 and RMSE values for the calibration curve using the sensel-by-sensel approach and for the three calibration fuctions proposed

	R2			**RMSE (kPa)**		
	min	**mean±std**	**max**	**min**	**mean±std**	**max**
Linear	0.82	0.94±0.01	0.99	0.15	1.11±0.58	5.3
2nd order	0.82	0.94±0.01	0.995	0.15	1.07±0.57	5.34
Power law	0.82	0.94±0.01	0.995	0.15	1.08±0.57	5.4

Table 3: RMSE of the pressure integral acting on each sensel for the three calibration functions proposed

	RMSE [N]		
	min	**mean±std**	**max**
Linear	0.0012	1.47±1.23	6.7
2nd order	0.0021	1.49±1.23	6.72
Power law	0.0053	1.49±1.23	6.7

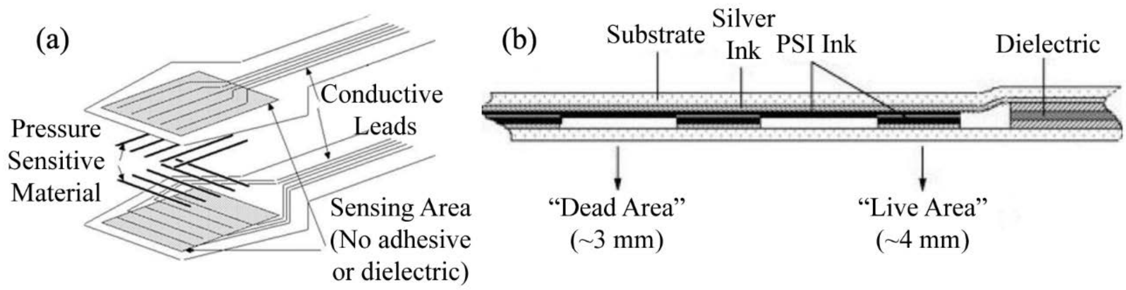

Figure 1: (a) Sketch illustrating the two sensor substrates, the pressure sensitive ink rows and columns and (b) schematic illustration of the sensor's cross section; reproduced from Tekscan, (2008).

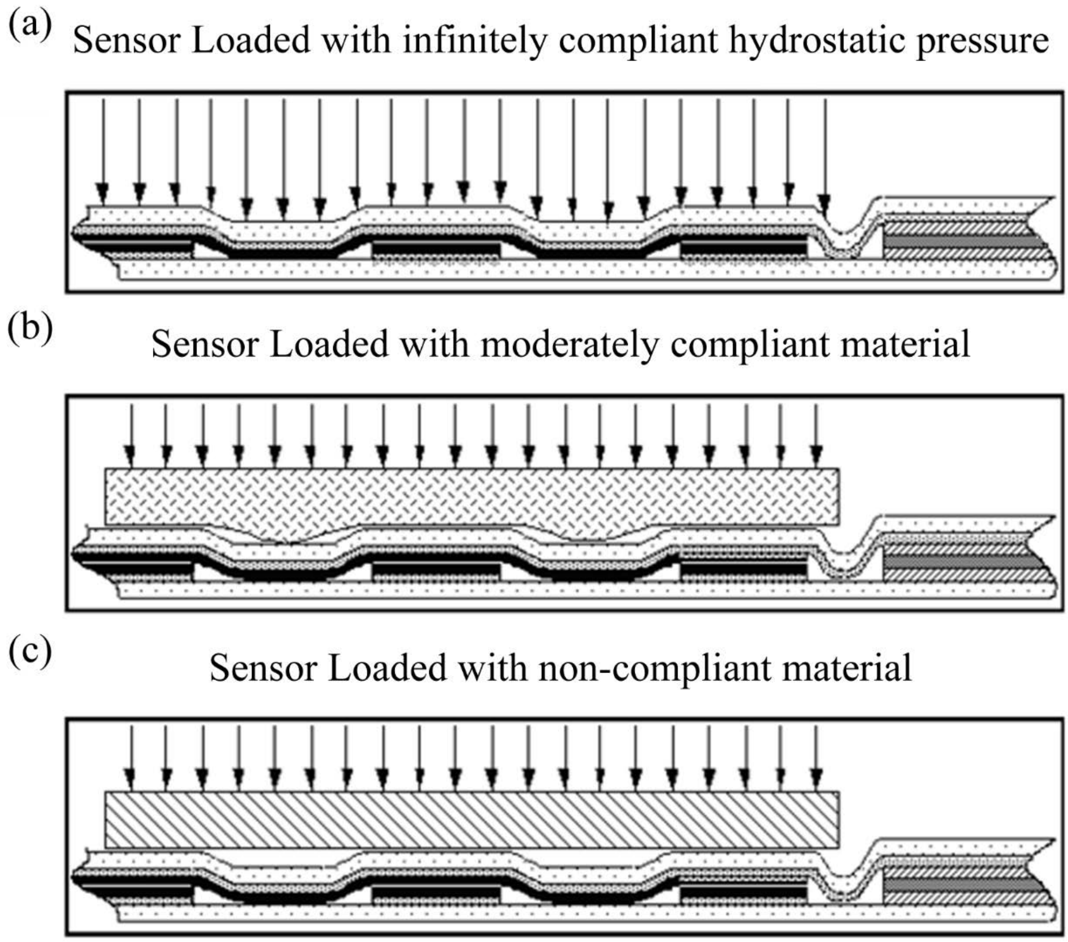

Figure 2: Examples of the pressure distribution on the sensor for (a) infinitely compliant material, (b) moderately compliant material, and (c) non-compliant material; reproduced from Tekscan (2008).

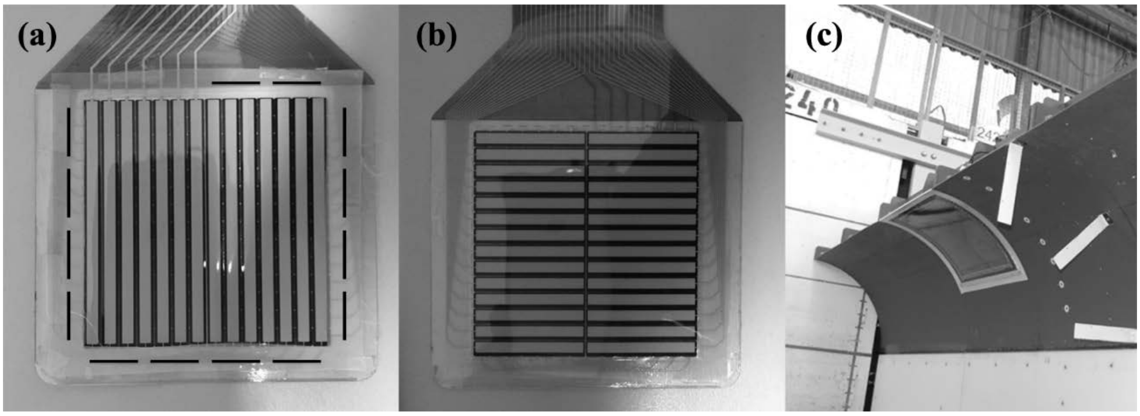

Figure 3: (a) Front. Black lines highlighting the cuts performed on the sensor to allow a proper ventilation. (b) Back image of the 9500 tactile sensor. (c) Underside of recurved crown seawall with a 4550 tactile sensor fixed on it, as built for a large scale physical model in Stagonas et al. (2014)

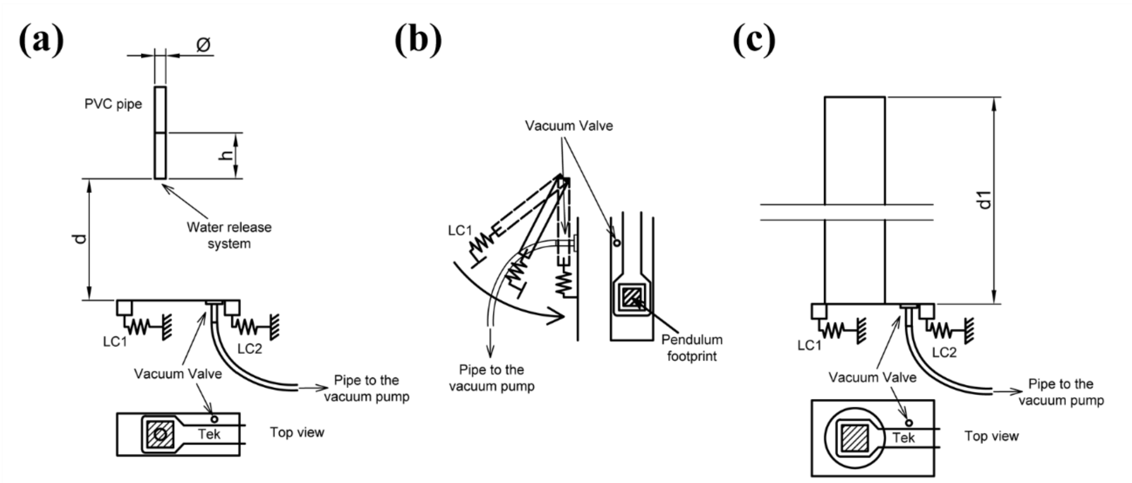

Figure 4: The three versions of the proposed experimental apparatus employing (a) water jets, (b) controlled pendulum, and (c) water column to induce dynamic and static pressures on the sensor.

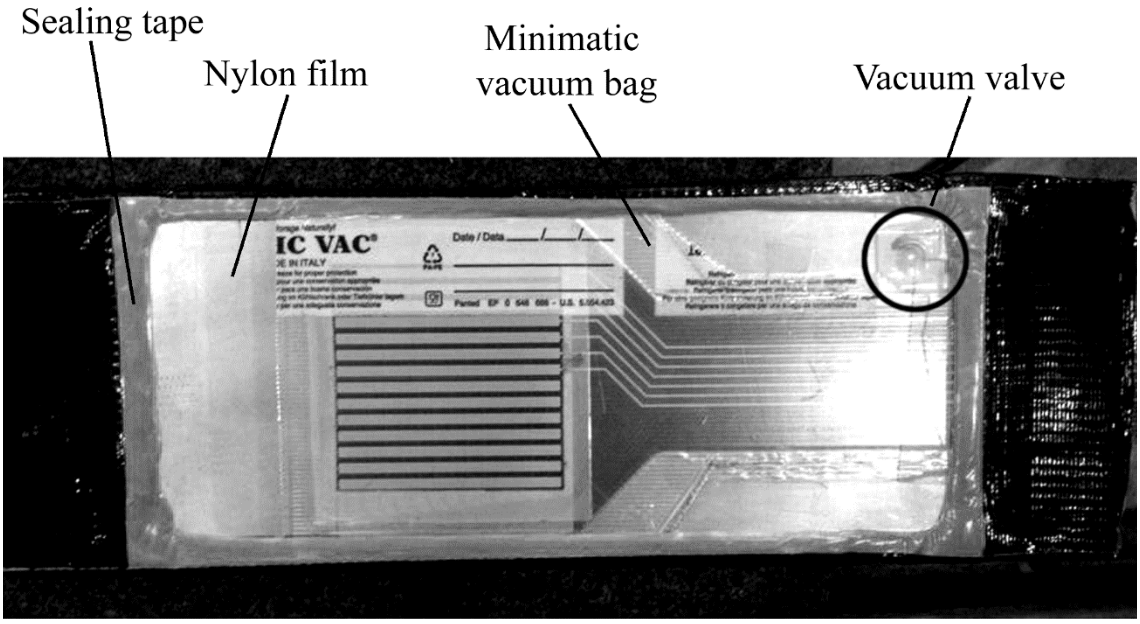

Figure 5: Experimental arrangement to prevent direct contact between sensor and water. The vacuum valve, the vacuum bag, the nylon film and the sealing tape are clearly displayed.

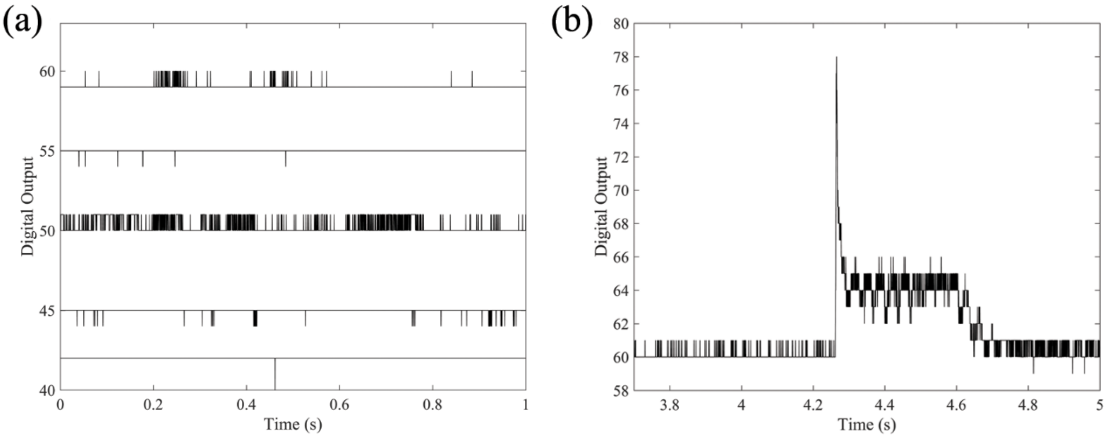

Figure 6: Time history examples of the digital output of a sensel subject to (a) static and (b) dynamic loads.

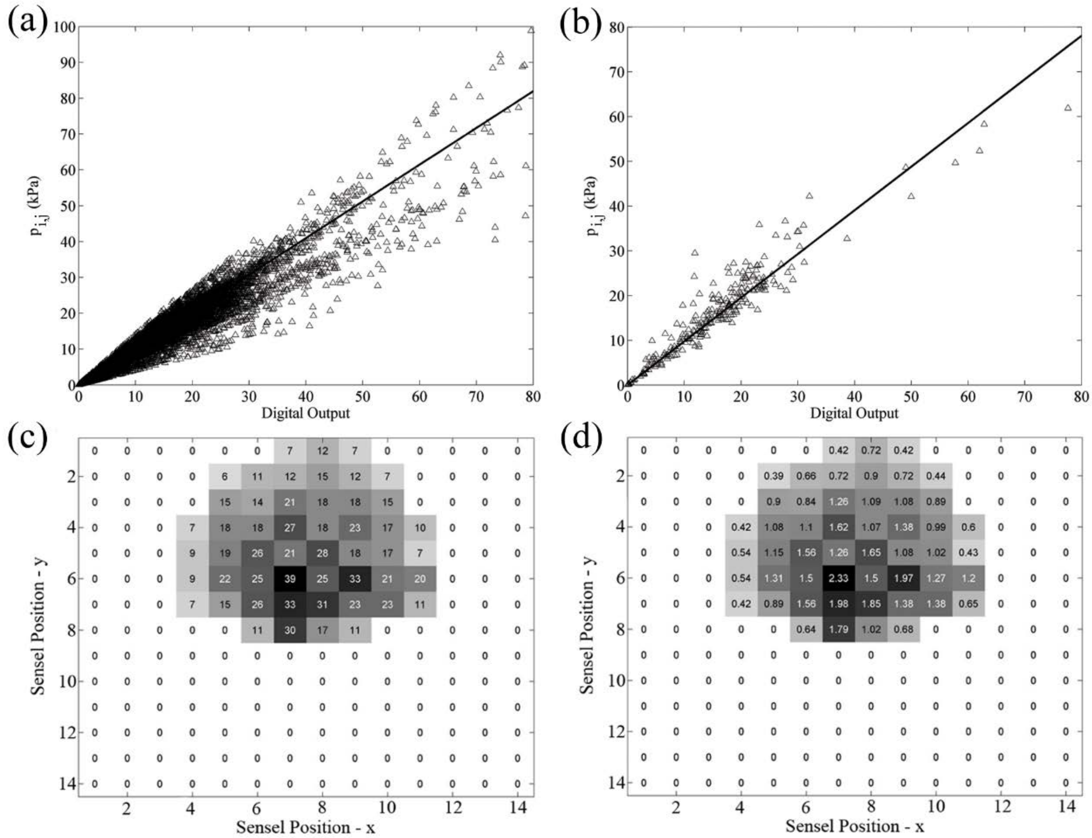

Figure 7: (a) Weighted peak pressures plotted over the digital output of all sensels, corresponding to the data set used for global calibration. (b) Weighted peak pressures over the digital output of a single sensel (i=8, j=10) as an example of the data set used for the sensel-by-sensel calibration. A linear function (black solid line) has also been fitted to the data of (a) and (b). Some examples of the (c) digital output and (d) weighting factor distribution are here presented as a 14×14 matrix.

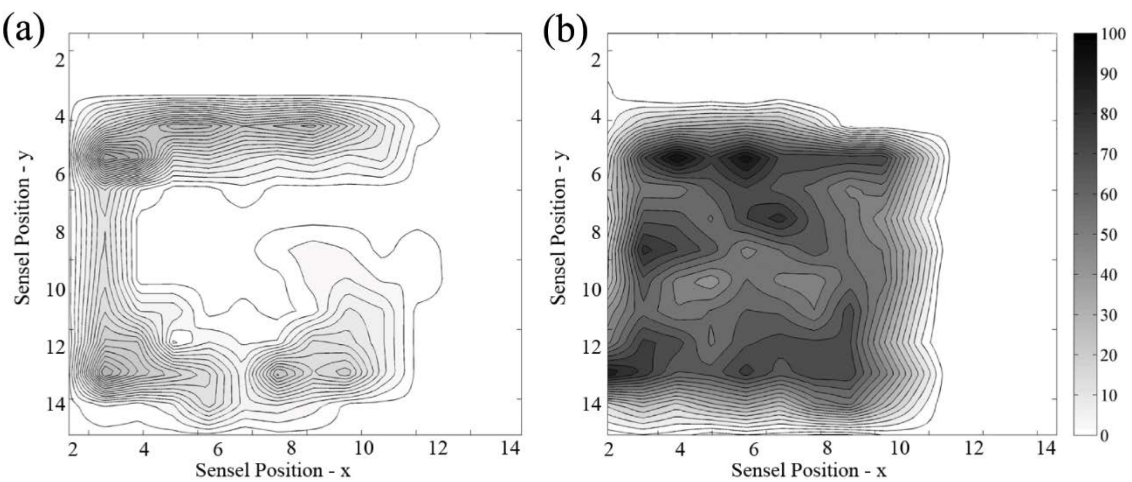

Figure 8: Contour plots of the pressure distribution for pendulum tests with (a) and without (b) entrapped air.

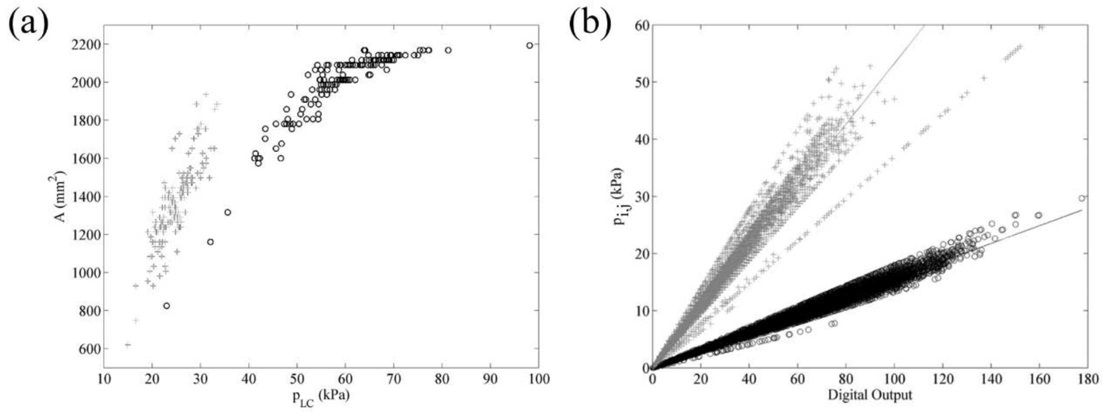

Figure 9: (a) Impact area recorded by the pressure mapping system for the non-perforated (crosses) and the perforated (circles) sensors, plotted over the peak of the mean pressure acting on the sensor. (b) Weighted pressure ($P_{i,j}$) plotted over the digital output of all sensels for the tests using the pendulum. Grey crosses: tests with air trapped in the sensor, black circles: tests with the air removed from the sensor.

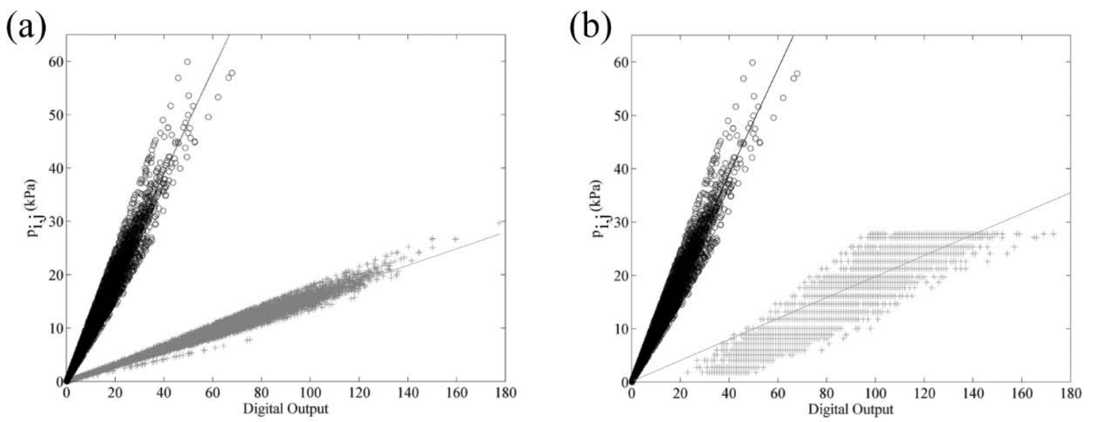

Figure 10: Weighted pressure ($P_{i,j}$) plotted over the digital output of all sensels for (a) the tests using the pendulum (grey crosses) and water jets (black circles), and (b) the tests using the water column (grey crosses) and water jets (black circles). Solid lines in (a): linear function fitted to the data from all sensels. Solid lines in (b) linear function fitted to the data of all sensels. Dashed line in (b): linear function fitted to the data from equilibrated sensels only.

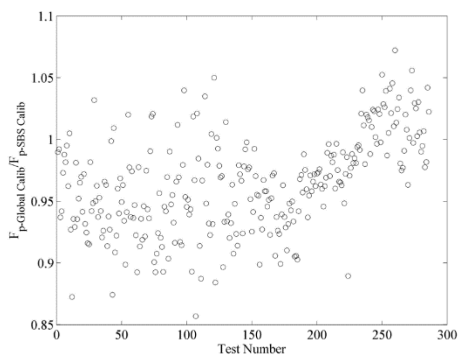

Figure 11: Ratio of the applied force peak calculated using a global and a sensel-by-sensel calibration for all test cases.

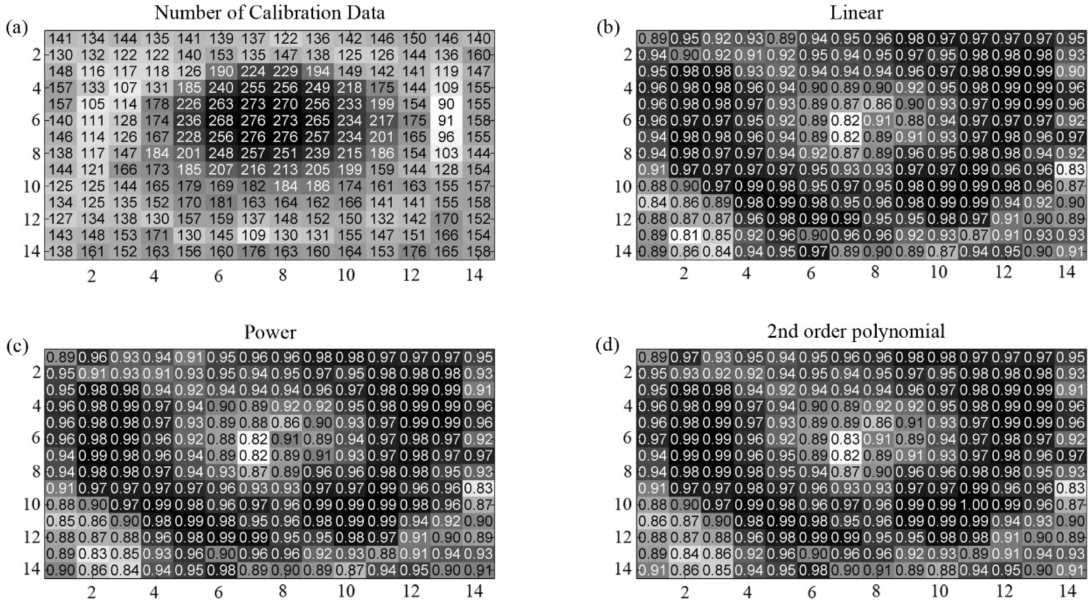

Figure 12: From top left and moving clockwise – (a) number of calibration data per sensel and R^2 per sensel for (b) linear calibration, (c) power law calibration and (d) 2nd order polynomial calibration; white in the colour scale corresponds to the smallest and black to the largest values.

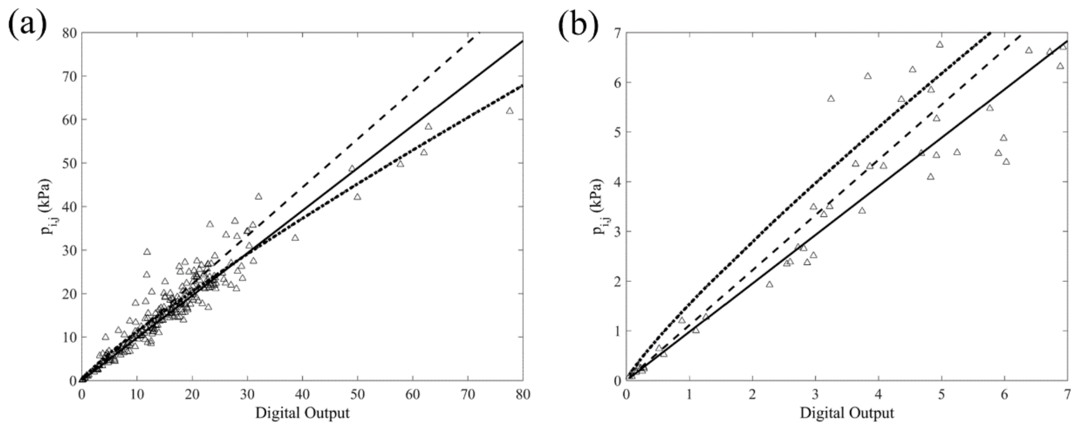

Figure 13: (a) Linear (solid line), power law (dotted lines) and 2^{nd} order polynomial (dashed lines) lines fitted to the data for a single sensel and (b) close-up view of the fits at the lower bound of the calibration range.

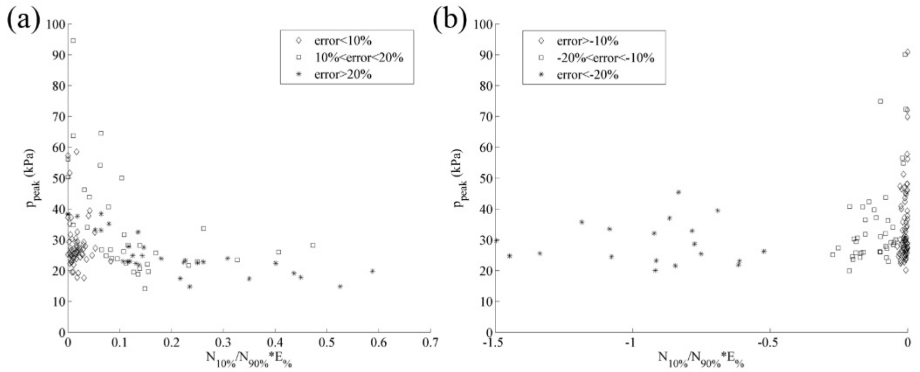

Figure 14: Plot of the pressure peaks recorded by a sensel for a given impact over $\frac{N_{10\%}}{N_{90\%}} * E_{\%}$ (Eq. 6) for (a) positive and (b) negative errors. The minimum, mean±std, and maximum error for the linear, power and 2nd order functions were -38%, 0.85±15.84% and 44.2%, -37%, 0.98±15.8% and 43.7%, and -37%, 0.8±15.4% and 42.8% (respectively).